Interseismic deformation fingerprints on the hyperarid coastal landscape in North Chilean subduction

Ehsan Kosari[1*], Sabrina Metzger[1], Victor Navarro-Sanchez[2], Onno Oncken[1], Bernd Schurr[1], Matthias Rosenau[1]

1 Helmholtz Centre Potsdam, GFZ German Research Centre for Geosciences, Potsdam, Germany

2 German Aerospace Center (DLR), Oberpfaffenhofen, Germany

* ehsan.kosari@gfz-potsdam.de; sabrina.metzger@gfz-potsdam.de; Victor.NavarroSanchez@dlr.de; onno.oncken@gfz-potsdam.de; bernd.schurr@gfz-potsdam.de; matthias.rosenau@gfz-potsdam.de

Interseismic deformation fingerprints on the hyperarid coastal landscape in North Chilean subduction

Ehsan Kosari[1*], Sabrina Metzger[1], Victor Navarro-Sanchez[2], Onno Oncken[1], Bernd Schurr[1], Matthias Rosenau[1]

1 Helmholtz Centre Potsdam, GFZ German Research Centre for Geosciences, Potsdam, Germany

2 German Aerospace Center (DLR), Oberpfaffenhofen, Germany

* ehsan.kosari@gfz-potsdam.de

Abstract

Along-strike seismotectonic behavior of subduction megathrusts feeds back into the forearc deformation as elastic and permanent deformation. However, whether and how short-term elastic deformation reflects long-term permanent deformation in the forearc and shapes the coastal region remains unclear. To evaluate the forearc deformation, we analyze the interseismic surface deformation obtained from six years of Sentinel-1 InSAR time series along the North Chilean Forearc (between 21.5°S to 26°S latitude), a hyperarid region where erosional processes masking topographic signals are minimized. To assess the conversion of interseismic vertical deformation into permanent deformation, we examine the spatial correlation between geodetic (short-term) vertical deformation and geomorphic (long-term) uplift markers and topography along the coast and Coastal Cordillera. Our findings reveal that the correlation between geodetic uplift rates and long-term uplift markers becomes neutral at the Mejillones Peninsula, suggesting localized tectonic activity. The Peninsula also separates two distinct seismotectonic segments with differing deformation patterns in the North and South. In the Northern segment, correlations and anticorrelations between geodetic uplift rates and geomorphic features imply episodic uplift, while upper plate faults exhibit less strain accumulation compared to the Southern segment and the Peninsula. The correlation variation may result from short-term, short-wavelength processes, while the consistently positive correlations with topography likely reflect long-term, long-wavelength deformation, overshadowing seismic-cycle short-wavelength deformation.

1 Introduction:

The dynamics of stress buildup and release govern the subduction seismic cycle (e.g., Savage, 1983) and cause elastic, viscoelastic, and permanent deformation in the upper plate (e.g., Wang et al., 2012; Baker et al., 2013; Kosari et al., 2023). As tectonic plates converge, the subducting plate descends beneath the upper plate, creating frictional resistance along the interface. This friction accumulates stress in locked zones (i.e., asperities; Lay and Kanamori, 1981) that steadily increase during the interseismic period, while adjacent areas experience gradual deformation. This cycle squeezes and stretches the upper plate primarily elastically, causing temporary uplift or subsidence (Figure 1a). Many seismic cycles may lead to some lasting changes in the upper plate (i.e., permanent deformation, e.g., Saillard et al., 2009; Melnick, 2016), manifested as crustal thickening and topography.

The whole slip spectrum of a seismic cycle occurring on the subduction interface (megathrust) plays a crucial role in vertical surface deformation, influenced by processes such as erosion and deep geological activities. In a homogenous medium, the amplitude and spatial extent of surface deformation depend on the rate vector of slip/backslip, particularly towards the down-dip end of the megathrust (e.g., Avouac, 2015). For short timescales (Figure 1b), coseismic surface displacements and interseismic surface deformation rates (Figure 1a) have been analyzed to determine the distribution of slip and slip deficit along the megathrust to locate asperities and assess their seismic potential (e.g., Moreno et al., 2010; Loveless and Meade; 2011). On the longer timescales, morphotectonic features are formed over hundreds of thousands of years (Figure1b) and have been suggested as a proxy to infer the distribution of slip and locking along megathrusts (e.g., Saillard et al., 2017; Malatesta et al., 2021). Forearc basins, often associated with locked regions and megathrust earthquakes, show gravity and topography anomalies (Song and Simons, 2003; Wells et al., 2003) that indicate patterns of long-term subsidence over multiple seismic cycles (e.g., Kosari et al., 2022a). Moving toward the shoreline, the edge of the continental shelf generally corresponds with the lower boundary of fully locked megathrust segments (e.g., Malatesta et al., 2021). In the coastal region, marine terraces provide records of Quaternary uplift rates that can be correlated with interseismic uplift rates (e.g., Saillard et al., 2017; Jolivet et al., 2020).

The correlation between short-term elastic deformation and long-term permanent deformation is often interpreted as an expression of the unbalanced nature of the earthquake deformation cycle. Recent advances in tectonic geodesy (Figure 1b) enable us to monitor decades-long surface deformation. Radar interferometric (InSAR) observations provide high-resolution surface deformation maps that can be combined with pointwise, accurate positioning of the Global Navigation Satellite System (GNSS) to derive three-dimensional deformation rate patterns (Weiss et al., 2020; Metzger et al., 2021; Ou et al., 2022). These observations highlight the short-term adjustments in land elevation due to elastic strain accumulation and release during the seismic cycle. On longer timescales (Figure 1b) and multiple seismic cycles, geomorphological studies provide substantial insights into landscape evolution in response to tectonic uplift (e.g., Cattin and Avouac, 2000; Marshall and Anderson, 1995). Land uplift influences erosion rates and the reorganization of drainage networks over geologic time, shaping the dynamic response of landscapes (Kirby and Whipple et al., 2012). This long-term perspective reveals how topographic features such as wind gaps and river terraces reflect both ongoing uplift processes and the cumulative effects of erosion and sediment transport. Integrating tectonic geodesy and geomorphological approaches allows untangling landscape dynamics across varying timescales (Figure 1b). While instrumental records provide precise measurements of short-term deformation, geomorphological archives extend our understanding over millennia, overcoming the limitations of shorter observational windows.

To examine how interseismic deformation influences coastal landscapes, we analyze secular geodetic data on the coast and Coastal Cordillera of the hyperarid Atacama region in the North Chilean Forearc. The North Chilean subduction zone, characterized by a sediment-starved trench, is notable for its minimal along-strike climate gradient (e.g., Strecker et al., 2007), a well-documented historical and instrumental large earthquake (e.g., Ruiz and Madariaga, 2018), distinct seismotectonic segmentations of the megathrust (e.g., Saillard et al., 2017), and active fault systems that run both parallel (Atacama fault system) and perpendicular to the trench (e.g., Victor et al., 2018; González et al., 2015).

We tie displacement rates obtained from six years of Sentinel-1 InSAR time-series and two view directions to a uniform reference frame spanned by accurate positioning rates (Figure 1c-d). We evaluate the correlation coefficient between ongoing deformation and topography. To assess the contribution of interseismic vertical deformation into permanent deformation along the coast and Coastal Cordillera, we examine the correlation between permanent uplift signatures (Figure 1e-h) from available uplifted marine terraces, coastal alluvial fans, topography, and river profiles.

2 Data and Methodology

2.1 Geodetic Surface Deformation and Strain Rates

We use Persistent-scatterer interferometry to monitor surface deformation by analyzing the changes in phase-stable point targets (PS) over time. These PS exhibit consistent and strong reflectivity in Synthetic Aperture Radar (SAR) images acquired along the line-of-sight (LOS) of the satellite between 2015 and 2020. The PS time-series analysis allows the measurement of deformation rates with millimeter accuracy over hundreds of kilometers along the satellite's ground track. We use four descending and three ascending tracks of the Sentinel-1 satellite (Figure 1c-d) covering North Chile. The PS processing uses the Integrated Wide Area Processor (IWAP) of the German Space Agency (Rodriguez Gonzalez et al., 2013; Plattner et al., 2022), designed to handle large areas and detect large-scale deformation. Given the arid and sparsely vegetated nature of North Chile, the backscattered signal is highly coherent over time, allowing for effective use of PS measurements (De Zan et al., 2010). The interferometric phases are corrected for ionospheric effects, solid earth tides, and tropospheric delays using CODE ionospheric data, IERS 2010 convention for solid earth tides, and ECMWF ERA-5 weather data, sampled in 30 km and 1 hr (Cong 2014; Cong et al. 2018; Rodriguez Gonzalez et al., 2018). These corrections allow for precisely calculating radar phase delays through the atmosphere and ionosphere. Following these corrections, the interferometric phase is unwrapped in time using base functions to account for deformation and residual topography components and then unwrapped in space for the remaining residuals (e.g., Plattner et al., 2022 and therein).

Following the approach by Metzger et al. (2021) based on Ou et al. (2022), we transform all individual LOS rate maps with their respective stable reference points into the South America reference frame using published horizontal GNSS data (e.g., Métois et al., 2013; Hoffmann et al., 2018). Each rate map is adjusted to fit the stable South America reference frame (DeMets et al., 1994) by applying a linear ramp that minimizes the misfit to (1) the horizontal GNSS rates (collapsed into LOS) within a specified station search radius of ~ 5 km and (2) the along-track radar-frame overlap. We, therefore, invert an over-determined design matrix weighted by the relative standard deviation of each data point in a search radius of ~ 5 km. The ascending and descending LOS observations can be decomposed into East and sub-vertical components (e.g., Fialko et al., 2001; Wright et al., 2004). The minor North component to which the right-looking satellite is least sensitive (~10%) can be suppressed by subtracting interpolated GNSS North rates from the sub-vertical data (Ou et al., 2022).

To compute strain rates, we employ a smoothing interpolator constrained by elasticity, which links the two horizontal velocity components (Sandwell & Wessel, 2016). The 2-D velocity is utilized to calculate the elasticity Green's functions and to compute the magnitude (second invariant) of the horizontal strain rate (Savage et al., 2001; Sandwell & Wessel, 2016).

2.2 Geodetic Slip Inversion

We apply a backslip model (Savage, 1983) to the ascending and descending InSAR rates and the GNSS rates to quantify the extent and amount of locking, respectively, secular slip along the plate interface. The backslip rate is constrained between 0 and 70 mm/a, representing freely slipping and fully locked areas, respectively. Kinematic fault locking is described as the fraction of plate convergence, ranging from 65mm/a to 75mm/a (e.g., Angermann et al., 1999; Norabuena et al., 1998), not accommodated by interseismic slip, which is calculated by dividing the estimated backslip rate by the plate convergence rate. Consequently, the locking degree ranges from 0% for areas where plate convergence is accommodated by free slip to 100% for areas of full locking. The plate interface is represented by the SLAB2.0 model (Hayes, 2018), discretized into triangular patches with a mean size of 10 km^2. The surface response on the slip on each patch is calculated by Green's functions of elastic dislocation in a half-space (Meade, 2007; Nikhoo and Walter, 2015), with two slip unit vectors with a rake of 30 and 90 degrees per patch. These vectors limit the horizontal azimuthal motion of each patch. The inversion problem is formulated as a Tikhonov-damped, bounded, weighted least-squares problem (e.g., Moreno et al., 2018).

2.3 Morphotectonic and Topographic Features

2.3.1 Topographic and River profiles

To compare geodetic vertical rates and topography, we use the 90m Space Shuttle Radar Topography (Farr et al. 2007) and extract 5-, 20-km-wide ~NS-profiles along the coast and the Coastal Cordillera, respectively.

River profiles cutting through the Coastal Cordillera and coast serve as key indicators of the long-term geological evolution of the region. The drainage network provides insights into uplift history and tectonic activity. Dating fluvial features in the Atacama Desert requires tracing their origins back to the Miocene period (e.g., Dunai et al., 2005; Nishiizumi et al., 2005). To draw river profiles using TopoToolbox (Schwanghart and Scherler, 2014), we first calculate the flow directions from a digital elevation model (DEM). We preprocess the DEM to carve outflow paths, ensuring that the flow direction network is well-defined and that pits or sinks are eliminated in the terrain. We then compute the flow accumulation grid, which indicates the drainage area in each DEM cell. Cells with higher flow accumulation values signify larger upstream flow, effectively identifying potential river channels. A stream network is created based on the flow direction. By defining a minimum contributing area, only cells with significant drainage are considered part of the stream network, thereby delineating the river network and filtering out minor tributaries. The final stream network is refined by retaining only the 50 largest connected stream networks, representing the main river networks, while less significant streams are discarded.

2.3.2 Geomorphic Features

2.3.2.1 Coastal Alluvial Fan Gradients

We use the fan gradient (g_f) as a geomorphometric marker to measure the correlation between along-strike variations of the geodetic vertical rates and the alluvial fan slopes (e.g., Giles, 2010). The values for North Chile have been calculated by Walk et al. (2020) using an empirical relationship that relates the fan gradient to the catchment area (A_c), expressed as ($gf = k\ A_c^{-b}$), where k and b are empirically derived constants (e.g., Giles, 2010; Walk et al., 2020). In regions with high recent uplift rates, rivers transport large amounts of sediments quickly from mountainous areas to the lower-elevation plains or basins (e.g., Clubb et al., 2023). This results in higher fan gradients (g_f) because the sediments are deposited more abruptly and over shorter distances where the rivers exit the mountainous terrain. The rapid deposition and steepening of the fan slope reflect the energetic processes driven by the high sediment supply and transport capacity. High uplift rates often create larger catchment areas as erosion carves out larger drainage basins. Larger catchment areas, combined with high sediment supply, further contribute to steeper fan gradients (g_f) because more sediments are available for deposition over a broader area. In hyperarid North Chile with extremely low precipitation rates and gradients (e.g., Houston, 2006), sediment availability is minimal (e.g., Madella et al., 2016). Hence, a lack of sediment supply and fast uplift can lead to steeper fan gradients (g_f) because the transported sediments are deposited quickly and locally, leading to steep slopes near the source areas.

2.3.2.2 Marine Terraces

Stair-cased marine terraces serve as dependable long-term records of historical sea-level highstands. Since current sea levels exceed those recorded since the early Pleistocene, any Pleistocene coastal feature above today's sea level indicates tectonic uplift (Lajoie, 1986). In North Chile, Pleistocene marine terraces formed in periods of relative seal-level highstand during interglacial and interstadial periods that coincided with the coastal uplift (e.g., Ortlieb et al., 1996; Martinod et al., 2016). The Quaternary oxygen-isotope curve, which distinguishes between warm and cold periods, shows that higher Quaternary Sea levels correlate with warmer periods, indicated by odd-numbered Marine Isotope Stages (MISs) (Lajoie, 1986; Shackleton et al., 2003). The well-preserved MIS 5e terrace level, known for its lateral continuity and high preservation potential, has been extensively used as a marker for correlating uplifted coastal areas. MIS 5e marine terraces in North Chile exhibit a variable elevation pattern, reflecting spatiotemporally variable uplift rates along strike over the past million years. Here, we use the marine terrace elevations of the last interglacial calculated by Freisleben et al. (2021; refer to detailed analysis therein).

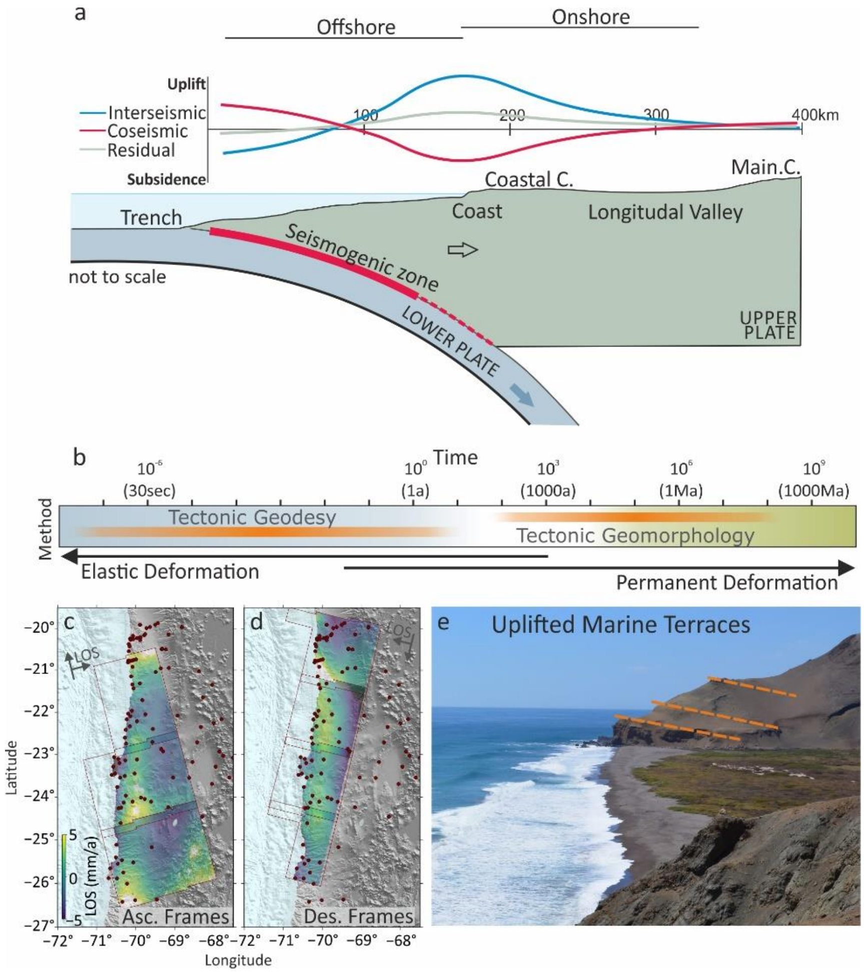

Figure 1: (a) Seismotectonic scheme of a simplified subduction system and surface uplift over the seismic cycle. (b) Observational time window and deformation style measured by tectonic geodesy and tectonic geomorphology. (c) and (d) show ascending and descending line-of-sight (LOS) deformation rates, respectively. Each ground track (marked by polygons) is in its internal reference frame. The red dots indicate the GNSS stations used in this study. (e) Examples of uplifted marine traces in North Chile.

2.4 Dataset Correlation analysis

We calculate the strength and direction of linear correlation between short- and long-term records by the Pearson correlation coefficient. This is the ratio between the covariance of two datasets and the product of their standard deviations, calculated as spatial correlation using a moving window along the NS profiles. The coefficient ranges between -1 and 1, representing negative (anticorrelation) and positive (correlation) linear relationships, respectively. The sliding of the spatial moving window by a single data point allows us to observe how the correlation varies along strike and reduces the effect of single data points as the window slides and recalculates the coefficient, providing insights into changes in the trend and pattern of the coefficients. Given that the datasets we are comparing have varying spatial resolutions, we downsample the higher-resolution dataset by averaging the values within a search radius of approximately 1-2 km. The length of the window is a trade-off between the length of the window and the number of data points. To maintain a constant data point count, the moving window length varies from ~50 to ~250 km. This length correlates well with the slip extent of large earthquakes in North Chile (e.g., Chlieh et al., 2004; Schurr et al., 2012 and 2014).

3 Results and Interpretation

3.1 Short-term interseismic deformation

The East rate (Figure 2a) decays from high at the coast to low at the East and shows distinct along-strike variations North and South of the Mejillones Peninsula. From North to South, the East rate increases at -21.4°, where the 2020 Mw 6.2 Loa River earthquake occurred (Tassara et al., 2022), then decreases toward the South at -22.4°. Further South, the rate increases again, reaching a maximum between -24° and -26°.

The vertical rates show minimum and maximum values of ~ -5.5 mm/a at Mejillones Peninsula and ~ + 5 mm/a at the Coastal Cordillera. The rate strongly correlates with latitude, hence, distance from the trench (Figure SI). On top of this first-order signal, the rates also vary along the strike in the coast and Coastal Cordillera (Figure 2b). In general, the Coastal Cordillera shows uplift, with some along-strike variations, reaching a maximum of ~ +5 mm/a between -22.5° and -23°, where the East rate is at its minimum. Further South, the vertical rate increases to ~ +5 mm/a between latitudes -24° and -25° before gradually decreasing. Directly along the coastline, the vertical rate oscillates from mainly uplift (North of Mejillones Peninsula, between ~ -21.5° and ~ -23°) to mainly subsidence in the South of the Peninsula (between ~ -23.5° and ~ -26°). In the South of the Peninsula, the headlands experience subsidence, but this subsidence fades in the Bay. The Mejillones Peninsula exhibits the maximum subsidence of the whole study area.

The Salar del Carmen, Paposo, and El Salado fault segments are the most prominent upper-plate fault structures of the Atacama fault system (Figure 2b). East of the Mejillones Peninsula, the Cerro Fortuna segment, the Southern branch of the Salar del Carmen segment, correlates well with the uplift-to-subsidence transition, delineating the coastal subsidence zone. In the Southern segment, two branches of the Paposo fault – Bolfin-Jorgillo and Izcuna – mark the extent of the coastal subsidence zone between latitudes -24° and -25°. Additionally, a branch of the El Salado fault binds the subsidence in the headland. Our InSAR data do not cover the coast further South in two view angles to trace the limit of the subsiding region. However, there is no clear subsidence, except slightly around ~ -22°, in the coastal region North of the Mejillones Peninsula, nor a correlation between the change in vertical displacement rates and the Salar del Carmen fault.

The geodetically derived locking of the plate interface shows that the locking is predominantly confined to depths between 20 and 40km. The locking pattern also exhibits along-strike changes (Figure 2c). Consistent with the geodetic rates, the locking distribution suggests different patterns North and South of the Mejillones Peninsula. The down-dip of maximum locking in the Northern segment is shallower (i.e., offshore), while in the Southern part, it deepens and extends below the coastal line, except in the bay region.

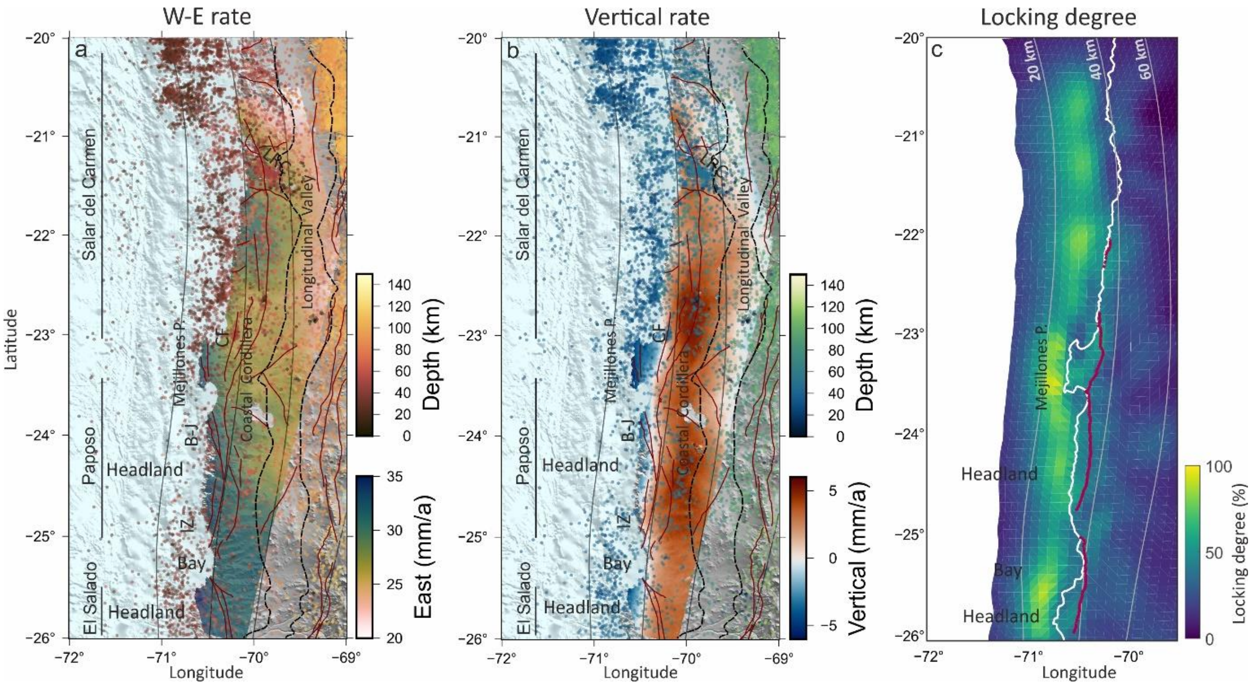

Figure 2: Decomposed East (a) and vertical (b) geodetic displacement rates relative to the stable South America reference frame. (c) Plate-interface locking map derived from the joint inversion of InSAR and GNSS observations. In all plots, contour lines represent the slab depth (SLAB 2.0 model; Hayes, 2018), and contour depths are labeled in panel (c). In (a) and (b), red lines indicate forearc faults, and in (c), mark uplift-subsidence hinge lines derived from vertical rates. The blacked dashed line indicates the extent of the Coastal Cordillera and Longitudinal Vally (Reutter et al., 2006). The seismicity catalog from the National Seismological Center of Chile (CSN 2013-2022) is plotted as dark red, resp. blue dots. LRC: Loa River Cluster; CF: Cerro Fortuna fault; B-J: Bolfin-Jorgillo fault; IZ: Izcuna fault. The arrow shows the location of the Loa River event and its aftershocks cluster.

Although there are no significant changes in the displacement rate visible along mapped upper-plate faults in the surface displacement rates, our residual LOS maps (Figure SI) and the strain rate map (second invariant of the strain; Figure 3) reveal that upper plate fault activity differs between the Northern and Southern segments. In the Northern segment, strain localizes only in the Cerro Fortuna segment and the northern termination of the Salar del Carmen segment on the Chomache fault. The Southern segment shows deformation concentrated in the Paposo and El Salado segments. On the Mejillones Peninsula, the strain rate map distinctly highlights the Cerro Moreno Fault (Eastern edge of the Peninsula) and the Mejillones Fault as two prominent lineaments.

3.2 Short-term vs. long-term deformation

The correlation between coastal topography and geodetic uplift rates (Figure 4a) is at its maximum in the latitudes between -20.5° and -22.5°. In this area, the geodetic vertical displacement rates are predominantly positive, meaning the region is uplifting. This strong correlation indicates that regions with higher coastal topography are undergoing more uplift. Moving Southward, the correlation diminishes while the correlation increases once the data North of the Loa River (approximately latitude -21.5°) is excluded. The correlation decreases gradually when data from the Mejillones Peninsula is included, such that there is no correlation, as the spatial correlation window only includes data points from the Peninsula. This neutral correlation indicates that the topography and vertical displacement in this region seem to be decoupled, meaning that topography does not linearly depend on interseismic vertical displacement rates. Further Southward, by gradually excluding the data points of the Peninsula, the correlation reaches its peak. In the Coastal Cordillera (Figure SI), topography and geodetic uplift rates exhibit their highest correlation, where both topography and vertical displacement rates show their highest values in the Northern segment (latitudes -22°). From -22.5° to -23.5°, there is no correlation between datasets. Moving Southward, (around latitudes -24° to -26°), however, the correlation again increases.

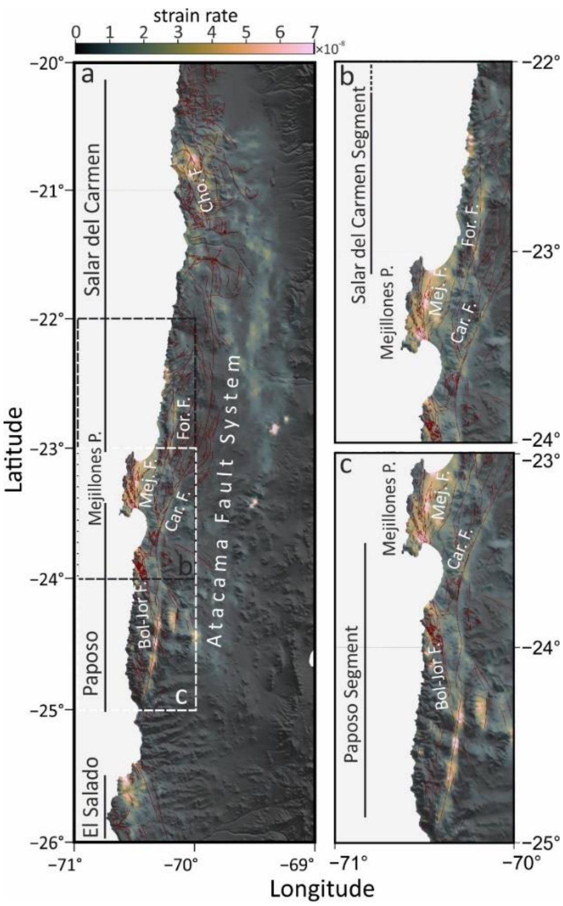

Figure 3: Strain rate map of the North Chilean Forearc. (a) The map depicts the strain accumulation along the Atacama Fault System, including, from North to South, Salar del Carmen, Mejillones, Paposo, and El Salado fault segments. The black and white dashed rectangles indicate the location of panels (a) and (b). The red lines represent the active faults of North Chile (Mittelstädt and Victor, 2020). Cho. F: Chomache Fault; For. F: Fortuna fault; Mej. F: Mejillones; Car. F: B-J: Bolfin-Jorgillo fault; IZ: Izcuna fault.

Coastal alluvial fans and marine terraces are proxies for uplift over shorter timescales compared to topographical changes (Figure 4b-c). The correlation coefficient between the elevation of marine terraces and interseismic vertical rates varies along the margin, demonstrating both correlation and anticorrelation (Figure 4b). In the Northern segment (latitude -20.5° to -22°), where geodetic uplift rates decrease towards the Mejillones Peninsula while marine terrace elevations increase, the datasets exhibit the highest anticorrelation. Excluding the data points around and North of Loa River shifts the high anticorrelation to a high correlation from -22° to -23. Including the data from the Mejillones Peninsula reduces the correlation and fluctuates the values, showing no linear relationship between marine terrace elevations and vertical displacement rates. The lack of correlation suggests that the elevations in the Peninsula are decoupled from the interseismic displacement rate, potentially due to localized tectonic activity such as faulting. Conversely, the anticorrelation is restored once the data points of the Mejillones Peninsula are excluded (from -23.8°) in the Southern segment, suggesting that higher marine terraces are associated with subsidence.

In the Northern region, specifically between -20.5° and -21.5° latitude, the datasets show a slight anticorrelation, meaning that as the slope gradient of coastal alluvial fans increases, the vertical displacement rates tend to decrease slightly (Figure 4c). Moving Southward, from -21.5° to -23° latitude, the datasets show a strong correlation by excluding the data North of Loa River. In this segment, an increase in slope gradient corresponds with a rise in vertical displacement rates, implying that areas with steeper slopes are associated with higher uplift rates. There is a data gap in the Mejillones Peninsula. However, in the Southern segment (from -24° latitude), the correlation between these two datasets diminishes, suggesting no linear relationship between interseismic vertical displacement rates and the slope of the coastal alluvial fans.

The river profiles reflect the cumulative uplift of different tectonic processes, including earthquake cycle deformation (refer to section 4.3 for discussion). While the river profiles (Figure 5a) in the Northern segment rarely (e.g., Loa River) cut through the Coastal Cordillera, they transverse the Coastal Cordillera in the Southern segments (Latitude -23.7° to -27.0°) and reach their outlet at the ocean. This allows us to check the lateral variation in the river profile (Figure 5b-c), where we have along-strike variation in geodetic rates and signs. Antofagasta River (Latitude: -23.7°) shows a concave profile except for the first 30-kilometer from the outlet, which shows a convex shape representation of a windgap. These profiles have gentler slopes compared to the rivers in the Bay and headland in the South. The river profiles in the bay show elevations, gradients, and shapes different from those of the Antofagasta River and adjacent headlands. The river profiles of the Bay area demonstrate a concave, steep, and upward-curving shape with significant elevation changes, particularly at short distances from the outlet. In the adjacent headlands, however, the river profiles show a concave shape, which is rather similar to the concave-shaped profile of Antofagasta River compared to the river profiles of the Bay. The elevation profiles are characterized by significant and consistent increases in elevation, extending across the entire distance.

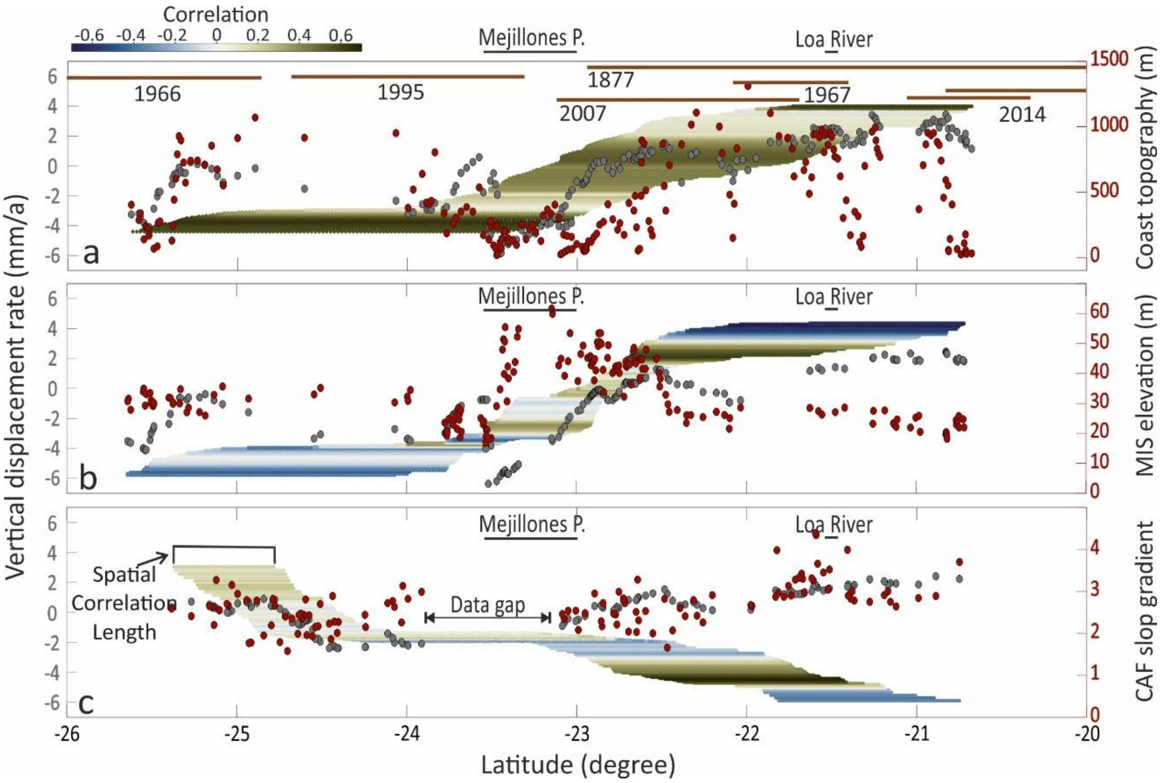

Figure 4: The spatial correlation coefficients between geodetic vertical rates (gary dots) and (a) coastal region elevation, (b) Marine Terraces elevation, and (c) coastal alluvial fan slope gradients. The spatial correlation length (color-coded band) indicates the lateral extent of data points used to calculate the correlation. The approximate locations of Mejillones Peninsula and Loa River are marked on the panels. The horizontal brown lines indicate the extent of the earthquakes in North Chile (Ruiz and Madariaga, 2018).

4 Discussion and Conclusion

4.1 Apparent discrepancy between short- and long-term dataset

The differences between the millimeter-scale geodetic uplift rates (e.g., this study and Jolivet et al., 2020) and the submillimeter-scale uplift rates derived from geomorphic markers (e.g., Melnick, 2016; Freisleben et al., 2021) along the margin can be understood in the context of temporal aliasing, where the resolution and timescales over which each dataset averages the vertical rate significantly impact the observed values (e.g., Sadler et al., 1981). Geodesy measures decade-long uplift rates with high temporal resolution, capturing short-term variations in vertical displacement, including subsidence due to elastic strain accumulation. These observations reflect a snapshot of the interseismic phase of the seismic cycle, leading to higher and more variable uplift rates, as well as instances of subsidence where elastic deformation temporarily outpaces uplift.

In contrast, geomorphic markers represent long-term geological records formed over millennia, integrating uplift over many seismic cycles. The geomorphic markers represent averaged rates, smoothing out decade-long variations and single subsidence events. As a result, marine traces and river profiles consistently show positive uplift values, reflecting the net uplift over extended periods, which incorporates both the interseismic uplift and the coseismic uplift that occurs during large earthquakes (e.g., Pedoja et al., 2014; Malatesta et al., 2022). The "aliasing effect" may explain why geodesy may show higher, more variable uplift rates and subsidence, while marine traces indicate a more consistent but lower uplift rate over longer timescales.

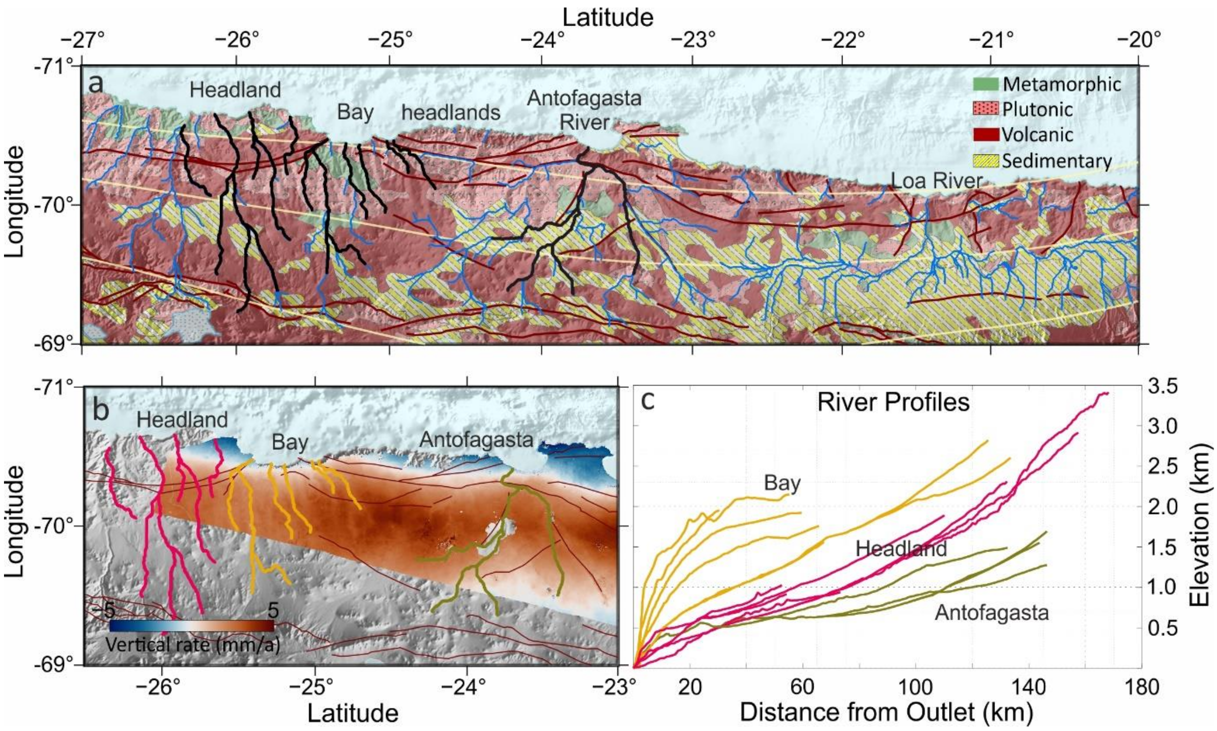

Figure 5: (a) Geological rock types (Gómez et al., 2019) overlaid by faults (dark red lines) and drainages (blue lines). The black lines indicate the river profiles highlighted (with different colors) in panel (b). Slab 40, 60, and 80 km contours are marked by yellow lines (b) Geodetic uplift rates in the Southern part of our study area, overlaid by faults (dark red lines) and drainages (blue lines). Profiles of the green, yellow, and magenta streamlines are shown in the river elevation profiles in (c).

4.2 Linking short-term observations to long-term records

Integrating short-term interseismic deformation with long-term geomorphological and geological records provides a better understanding of the tectonic processes shaping the coastal region. The geodetic rates reveal distinct along-strike rate changes in the East and vertical components, delineating two segments separated by the Mejillones Peninsula (Figure 2). These short-term deformation patterns align variably with long-term features such as coastal alluvial fan slopes and marine terrace elevation changes (Figure 4). However, topography, as geological-timescale markers, shows a different correlation pattern with the interseismic vertical rates than geomorphological-timescale. This difference highlights the contribution of other controlling factors in topography.

The correlation between geodetic vertical rates and geomorphic features, as well as topography, may reflect insights into the temporal and spatial dynamics of landscape evolution. Geomorphic features, which evolve on shorter timescales, are influenced by more rapid and localized processes subject to spatial variability, causing variations in uplift rate and sign. This variability may explain why the correlation between geodetic vertical rates and geomorphic features can be both positive and negative (anticorrelation). On the other hand, the correlation between geodetic vertical rates and topography is consistently positive, which can be attributed to the longer-term and more stable geological processes that shape long-wavelength deformation. The geodetic vertical rates show positive correlations with topography because areas of high relief are associated with a high geodetic uplift rate, and the areas with lower relief are associated with a low geodetic uplift rate or subsidence. This lack of anticorrelation in topographic profiles may suggest that while short-term localized subsidence occurs during the seismic cycle, they are overprinted by the larger-wavelength, long-term trends of tectonic uplift.

Distinct patterns emerge regarding how the correlation between vertical displacement rates and geomorphic features changes across latitudes (Figure 4). In the Northern segment between latitudes -20.5° and -22°, there is an anticorrelation between vertical displacement rates and geomorphic features (coastal alluvial fans and marine terraces). This anticorrelation suggests that a strong interseismic contributes to controlling the long-term deformation of the coastal region. In contrast, as we approach the Mejillones Peninsula, the correlations neutralize, suggesting that tectonic processes in this region are more localized or that other processes have a higher contribution to the deformation of the coastal region. This neutralization of the correlation aligns well with the localization of strain along the active faults in the Peninsula. However, limited knowledge of the fault geometry at depth, along with potential changes in fault behavior during the megathrust seismic cycle (e.g., Shirzaei et al., 2012; Victor et al., 2018; Kosari et al., 2022b), makes it challenging to exclude the role of faults in the short- and long-term deformation. Modeling is essential to uncover the impact of each major fault on surface displacement rates.

The Peninsula seems to act as a transition zone where the surface processes and tectonic movements are less directly linked to the larger-scale patterns observed North of it. South of the Mejillones Peninsula, the correlations remain weak between vertical displacement rates and coastal alluvial fans but trend toward negative values between vertical displacement rates and marine terrace elevations. This implies that in the Southern part, the elevated terraces are linked to subsidence, though other factors primarily influence the coastal alluvial fans. The spatial distribution of projected extreme precipitation for the Northern and Southern parts of the Peninsula aligns with the correlation values for coastal alluvial fans. According to the climate model (precipitation >2mm) for recurrence intervals of 50 years for the region (Walk et al., 2020), the Southern part is expected to receive significantly more precipitation than the North, ranging from 3 mm in the North to 63 mm in the South, highlighting the role of climate as a controlling factor.

The correlation between the geodetic vertical rates and changes in coastal alluvial fan slopes and marine terrace elevations indicates consistent uplift over shorter (i.e., seismic cycle) timescales. However, where this relationship declines into anticorrelation suggests episodic or non-uniform uplift patterns. The anticorrelation between geodetic and long-term records can be interpreted as a correlation to the coseismic vertical deformation signal of the opposite sign. Some of the significant additional factors beyond seismic cycle deformation that may influence long-term landscape development are discussed in section 4.3.

The down-dip limit of the high locking zone (Figure 2c) changes in the Northern and Southern segments, with the Mejillones Peninsula in the center. This impacts the elastic surface response as observed by geodesy. Assuming the locking remains stationary, the interseismic deformation rates fingerprint the long-term deformation recorded in the morphological markers. The transition in high locking depth from the Northern to the Southern segments corresponds to varying uplift rates. The uplift rate is more pronounced along the coast in the Northern segment, where the high locking depth is shallower. In the Southern segment, the high locking depth is beneath the coastline, and the geodetic uplift rate correlates with the lower elevation and gentler slope of the Antofagasta River (Figure 5c). Moving Southward, the shallower high locking depths near the Bay (Figure 2c) are reflected in the highly concave, steep profiles of rivers in the bay area (Figure 5c). These rivers exhibit significant elevation changes over short distances, indicating more dynamic and possibly episodic uplift over longer timescales. In the adjacent headlands, again, the locking depth is beneath the coastline, and the subsidence correlates with the lower elevations and gentler slopes of the Antofagasta River.

A non-steady long-term uplift rate has been suggested along the margin of North Chile, highlighting the influence of variable tectonic processes on marine terrace development (e.g., Melnick, 2016; Saillard et al., 2017; Freisleben et al., 2021). It has been suggested that uplift rates vary significantly over the Pleistocene, reflecting a non-steady interaction between tectonic processes and surface uplift. Our observed variations in uplift and subsidence patterns support these findings, suggesting that seismic-cycle episodic or non-uniform uplift rates are likely a common feature along the Chilean margin. Moreover, spatial variation in denudation rates in the Coastal and Western Cordilleras of Northern Chile suggest latitudinal variations in uplift rates along the margin (Starke et al., 2017) such that, in the North-South direction, the Coastal Cordillera denudation rates increase toward the South (from -20.5° to -22.5° latitude). Additionally, Jolivet et al. (2020) propose that interseismic loading of the subduction megathrust drives long-term uplift in Northern Chile. They suggest that areas of high long-term uplift correspond to regions of significant interseismic strain accumulation. Our results align with this hypothesis, as regions exhibiting short-term uplift/minimum subsidence correspond to areas of sustained long-term uplift (e.g., in the Bay region; Figure 5b-c), emphasizing the role of seismic cycle processes in shaping the long-term landscape.

4.3 Other contributors to the short-term uplift signal

4.3.1 Deep Sources

Another process governing surface uplift is underplating, where materials are accreted to the upper plate from the subducting slab and the base of the upper plate, which can lead to long-term (Ma-a) coastal topography (Clift and Hartley, 2007; Encinas et al., 2012). The vertical surface displacement rates caused by underplating may exceed 1 mm/a (e.g., Menant et al., 2020). Also, underplating may show subsidence or uplift episodes depending on its evolution stage, making it difficult to discriminate the signal from the elastic vertical rates (e.g., Menant et al., 2020; Angiboust et al., 2021). As the vertical rate sign changes South of Mejillones Peninsula over a short distance, also since the sign of the interseismic vertical rates changes with distance from the trench, the predominant component of the surface deformation signal may source from the interseismic locking on the subduction interface along the coast.

In the Coastal Cordillera, the wavelength of the observed uplift signal exceeds 100 km long- and 50 km across-strike (Figure 2b). This wavelength suggests a deep source near the plate interface. In addition, a hybrid underplating regime has been suggested for North Chile as underplating occurs onshore forearc at a depth of 30-50 km, synchronous with tectonic erosion in offshore forearc (Clift and Hartley, 2007; Angiboust et al., 2021). The suggested depth of underplating for North Chile favors the observed uplift in the Coastal Cordillera, where two possible underplatings have been proposed at depths > 35 km in the latitude of the Mejillones Peninsula and latitude -22.30 (Parraguez Landaeta et al., 2023). This evidence suggests the contribution of the other components, with different wavelengths, in the uplift pattern and rates of the Coastal Cordillera.

Long-term slip on deep, steep faults, such as the source of the Michilla 2007 event (e.g., Fuenzalida et al., 2013), may also contribute to the vertical motion of the Coastal Cordillera. Additionally, background seismicity associated with crustal thickening has been suggested to contribute to the uplift along active margins (e.g., Madella and Ehlers, 2021). A secondary zone of surface uplift, caused by coseismic events and afterslip, can also play a role in the uplift of the coast and Coastal Cordillera (e.g., Ragon and Simons, 2023; van Dinther et al., 2019). Despite their potential contribution, the predominant component of the ongoing surface signal in the coastal region remains the interseismic locking on the subduction interface.

4.3.2 Upper plate fault effect

The Cerro Fortuna, Bolfin-Jorgillo, and Izcuna fault segments also limit the extent of coastal subsidence (Figure 2b and 3), but to understand their role, a better examination of their slip types, dip directions, and displacement rates is essential. To contribute to coastal subsidence, the faults must exhibit either normal faulting on a westward dipping plane (as reported by Cembrano et al., 2005 for the Bolfin-Jorgillo fault), or reverse faulting on an eastward dipping plane. Conversely, it has been proposed that the Cerro Fortuna branch features a normal faulting component with an eastward dip direction (e.g., Victor et al., 2018). This orientation is less likely to produce a surface subsidence signal on its footwall in the vicinity of the Mejillones Peninsula, where the fault geometry does not support the observed subsidence patterns.

Paleoseismology suggests potential Mw 6.5-7.0 events for the Southern segments of the Salar del Carmen and Mejillones Faults with much longer recurrence intervals than megathrust events (Cortés-Aranda et al., 2012; Ewiak et al., 2014). Our residual LOS maps (Figure SI) and strain map (Figure 3) reveal the strain concentration and surface displacement at the fault trace, supporting the activity of the Salar del Carmen and Mejillones faults. The absence of a detectable displacement signal in the Northern segment, except the Chomache fault segment (Figure 3a), does not necessarily imply inactivity; rather, it may indicate that our dataset lacks the North-south sensitivity needed to capture the displacement rate along certain faults. Additionally, any movement in the Northern segment might be subtle enough to distinguish it from the significant surface displacement caused by interseismic locking on the subduction interface. This indicates that the displacement due to locking on the subduction interface might overshadow the contributions from upper-plate faults, complicating their measurement. Alternatively, these faults may not consistently follow the typical earthquake cycle (Cortés-Aranda et al., 2012), possibly being active only during specific portions of the cycle (e.g., González et al., 2021; Loveless et al., 2010; Victor et al., 2009). This complexity highlights the challenge of attributing surface deformation to a single cause. It is essential to employ modeling approaches to determine the effects of each major fault on surface displacement rates.

Seismotectonic laboratory experiments (e.g., Rosenau et al., 2009; Kosari et al., 2022b) suggest that the co-location of upper-plate faults with the surface transition from uplift to subsidence is plausible that these faults extend downwards to the down-dip end of the locking zone on the subduction interface. Such a configuration implies that these faults could be reactivated during seismic events, exhibiting different kinematic behaviors at various stages of the seismic cycle. During coseismic periods, these faults might exhibit normal mechanisms due to the sudden release of accumulated strain, leading to subsidence. In contrast, during interseismic periods, these faults might display reverse mechanisms as the region gradually accumulates strain, resulting in an uplift (Kosari et al., 2022b). This change in fault kinematics underscores the dynamic nature of fault behavior and its influence on surface deformation. The implications of this fault behavior are significant for understanding the long-term tectonic evolution of the region. The alternating extensional and compressional phases (e.g., Shirzaei et al., 2012) with a dominant sense of slip could contribute to the topography observed in the coastal region, with periods of subsidence followed by uplift. This mechanism could also explain the variability in short-term and long-term deformation patterns, as the fault system responds to the changing stress regime over multiple seismic cycles.

Acknowledgments

The authors appreciate the helpful discussions with M. Nikkhoo and J. Bedford. Some figures were created using GMT (Wessel et al., 2013), and some figures benefited from scientific colormaps (Crameri, 2020). The GNSS rate tables can be found as referenced in the text, while the rate maps and slip model will be openly accessible soon via GFZ Data Services.

References

Angermann, D., Klotz, J., & Reigber, C. (1999). Space-geodetic estimation of the Nazca-South America Euler vector. *Earth and Planetary Science Letters*, *171*(3), 329-334.

Angiboust, S., Menant, A., Gerya, T., & Oncken, O. (2022). The rise and demise of deep accretionary wedges: A long-term field and numerical modeling perspective. *Geosphere*, *18*(1), 69-103.

Avouac, J. P. (2015). From geodetic imaging of seismic and aseismic fault slip to dynamic modeling of the seismic cycle. *Annual Review of Earth and Planetary Sciences*, *43*(1), 233-271.

Baker, A., Allmendinger, R. W., Owen, L. A., & Rech, J. A. (2013). Permanent deformation caused by subduction earthquakes in northern Chile. Nature Geoscience, 6(6), 492-496.

Cattin, R., & Avouac, J. P. (2000). Modeling mountain building and the seismic cycle in the Himalaya of Nepal. *Journal of Geophysical Research: Solid Earth*, *105*(B6), 13389-13407.

Cembrano, J., González, G., Arancibia, G., Ahumada, I., Olivares, V., & Herrera, V. (2005). Fault zone development and strain partitioning in an extensional strike-slip duplex: A case study from the Mesozoic Atacama fault system, Northern Chile. *Tectonophysics*, *400*(1-4), 105-125.

Chlieh, M., De Chabalier, J. B., Ruegg, J. C., Armijo, R., Dmowska, R., Campos, J., & Feigl, K. L. (2004). Crustal deformation and fault slip during the seismic cycle in the North Chile subduction zone, from GPS and InSAR observations. *Geophysical Journal International*, *158*(2), 695-711.

Clift, P. D., & Hartley, A. J. (2007). Slow rates of subduction erosion and coastal underplating along the Andean margin of Chile and Peru. *Geology*, *35*(6), 503-506.

Clubb, F. J., Mudd, S. M., Schildgen, T. F., van der Beek, P. A., Devrani, R., & Sinclair, H. D. (2023). Himalayan valley-floor widths controlled by tectonically driven exhumation. *Nature Geoscience*, *16*(8), 739-746.

Cong, X. (2014). *SAR interferometry for volcano monitoring: 3D-PSI analysis and mitigation of atmospheric refractivity* (Doctoral dissertation, Technische Universität München).

Cong, X., Balss, U., Rodriguez Gonzalez, F., & Eineder, M. (2018). Mitigation of tropospheric delay in SAR and InSAR using NWP data: Its validation and application examples. *Remote Sensing*, *10*(10), 1515.

Cortés-Aranda, J., et al. "Normal upper plate fault reactivation in northern Chile and the subduction earthquake cycle: From geological observations and static Coulomb Failure Stress (CFS) change." *Tectonophysics* 639 (2015): 118-131.

Crameri, F. (2020). Scientific color maps. https://doi.org/10.5281/ZENODO.1287763

DeMets, C., Gordon, R. G., Argus, D. F., & Stein, S. (1994). Effect of recent revisions to the geomagnetic reversal time scale on estimates of current plate motions. Geophysical research letters, 21(20), 2191-2194.

Dunai, T. J., López, G. A. G., & Juez-Larré, J. (2005). Oligocene–Miocene age of aridity in the Atacama Desert revealed by exposure dating of erosion-sensitive landforms. *Geology*, *33*(4), 321-324.

Encinas, A., Finger, K. L., Buatois, L. A., & Peterson, D. E. (2012). Major forearc subsidence and deep-marine Miocene sedimentation in the present Coastal Cordillera and Longitudinal Depression of south-central Chile (38 30′ S–41 45′ S). *Bulletin*, *124*(7-8), 1262-1277.

Ewiak, O., Victor, P., & Oncken, O. (2015). Investigating multiple fault rupture at the Salar del Carmen segment of the Atacama Fault System (northern Chile): Fault scarp morphology and knickpoint analysis. *Tectonics*, *34*(2), 187-212.

Farr, T. G., Rosen, P. A., Caro, E., Crippen, R., Duren, R., Hensley, S., ... & Alsdorf, D. (2007). The shuttle radar topography mission. *Reviews of geophysics*, *45*(2).

Fialko, Y., Simons, M., & Agnew, D. (2001). The complete (3-D) surface displacement field in the epicentral area of the 1999 Mw7. 1 Hector Mine earthquake, California, from space geodetic observations. *Geophysical research letters*, *28*(16), 3063-3066.

Freisleben, R., Jara-Muñoz, J., Melnick, D., Martínez, J. M., & Strecker, M. R. (2021). Marine terraces of the last interglacial period along the Pacific coast of South America (1 N–40 S). Earth System Science Data Discussions, 2020, 1-39.

Fuenzalida, A., Schurr, B., Lancieri, M., Sobiesiak, M., & Madariaga, R. (2013). High-resolution relocation and mechanism of aftershocks of the 2007 Tocopilla (Chile) earthquake. *Geophysical Journal International*, *194*(2), 1216-1228.

Giles, P. T. (2010). Investigating the use of alluvial fan volume to represent fan size in morphometric studies. *Geomorphology*, *121*(3-4), 317-328.

Gómez, J., Schobbenhaus, C. & Montes, N.E., compilers. (2019). Geological Map of South America 2019. Scale 1:5 000 000. Commission for the Geological Map of the World (CGMW), Colombian Geological Survey, and Geological Survey of Brazil. Paris. https://doi.org/10.32685/10.143.2019.929

Gonzalez, F. R., Adam, N., Parizzi, A., & Brcic, R. (2013, December). The integrated wide area processor (IWAP): A processor for wide area persistent scatterer interferometry. In *ESA Living Planet Symposium* (Vol. 722, p. 353).

Gonzalez, F. R., Parizzi, A., & Brcic, R. (2018, June). Evaluating the impact of geodetic corrections on interferometric deformation measurements. In *EUSAR 2018; 12th European Conference on Synthetic Aperture Radar* (pp. 1-5). VDE.

González, G., Pasten-Araya, F., Victor, P., González, Y., Valenzuela, J., & Shrivastava, M. (2021). The role of interplate locking on the seismic reactivation of upper plate faults on the subduction margin of northern Chile. Scientific Reports, 11(1), 21444.

González, G., Salazar, P., Loveless, J. P., Allmendinger, R. W., Aron, F., & Shrivastava, M. (2015). Upper plate reverse fault reactivation and the unclamping of the megathrust during the 2014 northern Chile earthquake sequence. *Geology*, *43*(8), 671-674.

Hayes, G. P., Moore, G. L., Portner, D. E., Hearne, M., Flamme, H., Furtney, M., & Smoczyk, G. M. (2018). Slab2, a comprehensive subduction zone geometry model. *Science*, *362*(6410), 58-61.

Hoffmann, F., Metzger, S., Moreno, M., Deng, Z., Sippl, C., Ortega-Culaciati, F., & Oncken, O. (2018). Characterizing afterslip and ground displacement rate increase following the 2014 Iquique-Pisagua Mw 8.1 earthquake, Northern Chile. *Journal of Geophysical Research: Solid Earth*, *123*(5), 4171-4192.

Houston, J. (2006). Variability of precipitation in the Atacama Desert: its causes and hydrological impact. *International Journal of Climatology: A Journal of the Royal Meteorological Society*, *26*(15), 2181-2198.

Jolivet, R., Simons, M., Duputel, Z., Olive, J. A., Bhat, H. S., & Bletery, Q. (2020). Interseismic loading of subduction megathrust drives long-term uplift in northern Chile. *Geophysical Research Letters*, *47*(8), e2019GL085377.

Kirby, E., & Whipple, K. X. (2012). Expression of active tectonics in erosional landscapes. *Journal of structural geology*, *44*, 54-75.

Kosari, E., Rosenau, M., & Oncken, O. (2022a). Strain signals governed by Frictional-Elastoplastic interaction of the upper plate and shallow subduction megathrust interface over seismic cycles. *Tectonics*, *41*(5), e2021TC007099.

Kosari, E., Rosenau, M., Ziegenhagen, T., & Oncken, O. (2022b). Upper plate response to a sequential elastic rebound and slab acceleration during laboratory-scale subduction megathrust earthquakes. *Journal of Geophysical Research: Solid Earth*, *127*(9), e2022JB024143.

Kosari, E., Rosenau, M., Metzger, S., & Oncken, O. (2023). Along-strike seismotectonic segmentation reflecting megathrust seismogenic behavior. Geology, 51(8), 707-712.

Lajoie, K. R. (1986). Coastal tectonics. *Active tectonics*, 95-124.

Lay, T., & Kanamori, H. (1981). An asperity model of large earthquake sequences. *Earthquake prediction: An international review*, *4*, 579-592.

Loveless, J. P., & Meade, B. J. (2016). Two decades of spatiotemporal variations in subduction zone coupling offshore Japan. *Earth and Planetary Science Letters*, *436*, 19-30.

Loveless, J. P., Allmendinger, R. W., Pritchard, M. E., & González, G. (2010). Normal and reverse faulting driven by the subduction zone earthquake cycle in the northern Chilean fore arc. *Tectonics*, *29*(2).

Madella, A., & Ehlers, T. A. (2021). Contribution of background seismicity to forearc uplift. *Nature Geoscience*, *14*(8), 620-625.

Malatesta, L. C., Bruhat, L., Finnegan, N. J., & Olive, J. A. L. (2021). Co-location of the downdip end of seismic coupling and the continental shelf break. *Journal of Geophysical Research: Solid Earth*, *126*(1), e2020JB019589.

Marshall, J. S., & Anderson, R. S. (1995). Quaternary uplift and seismic cycle deformation, Peninsula de Nicoya, Costa Rica. *Geological Society of America Bulletin*, *107*(4), 463-473.

Martinod, J., Regard, V., Riquelme, R., Aguilar, G., Guillaume, B., Carretier, S., ... & Hérail, G. (2016). Pleistocene uplift, climate and morphological segmentation of the Northern Chile coasts (24 S–32 S): Insights from cosmogenic 10Be dating of paleoshorelines. *Geomorphology*, *274*, 78-91.

Meade, B. J. (2007). Algorithms for the calculation of exact displacements, strains, and stresses for triangular dislocation elements in a uniform elastic half space. *Computers & geosciences*, *33*(8), 1064-1075.

Melnick, D. (2016). Rise of the central Andean coast by earthquakes straddling the Moho. *Nature Geoscience*, *9*(5), 401-407.

Menant, A., Angiboust, S., Gerya, T., Lacassin, R., Simoes, M., & Grandin, R. (2020). Transient stripping of subducting slabs controls periodic forearc uplift. *Nature communications*, *11*(1), 1823.

Métois, M., Socquet, A., Vigny, C., Carrizo, D., Peyrat, S., Delorme, A., ... & Ortega, I. (2013). Revisiting the North Chile seismic gap segmentation using GPS-derived interseismic coupling. *Geophysical Journal International*, *194*(3), 1283-1294.

Metzger, S., Gągała, Ł., Ratschbacher, L., Lazecký, M., Maghsoudi, Y., & Schurr, B. (2021). Tajik depression and greater Pamir neotectonics from InSAR rate maps. *Journal of Geophysical Research: Solid Earth*, *126*(12), e2021JB022775.

Mittelstädt, J., & Victor, P. (2020). Active fault database for the Atacama Fault System (N-Chile) as basis for tracking forearc segmentation.

Moreno, M., Li, S., Melnick, D., Bedford, J. R., Báez, J. C., Motagh, M., ... & Oncken, O. (2018). Chilean megathrust earthquake recurrence linked to frictional contrast at depth. *Nature Geoscience*, *11*(4), 285-290.

Moreno, M., Rosenau, M., & Oncken, O. (2010). 2010 Maule earthquake slip correlates with pre-seismic locking of Andean subduction zone. *Nature*, *467*(7312), 198-202.

Nikkhoo, M., & Walter, T. R. (2015). Triangular dislocation: an analytical, artefact-free solution. *Geophysical Journal International*, *201*(2), 1119-1141.

Nishiizumi, K., Caffee, M. W., Finkel, R. C., Brimhall, G., & Mote, T. (2005). Remnants of a fossil alluvial fan landscape of Miocene age in the Atacama Desert of northern Chile using cosmogenic nuclide exposure age dating. *Earth and Planetary Science Letters*, *237*(3-4), 499-507.

Norabuena, E., Leffler-Griffin, L., Mao, A., Dixon, T., Stein, S., Sacks, I. S., ... & Ellis, M. (1998). Space geodetic observations of Nazca-South America convergence across the central Andes. *Science*, *279*(5349), 358-362.

Ortlieb, L., Zazo, C., Goy, J., Hillaire-Marcel, C., Ghaleb, B., & Cournoyer, L. (1996). Coastal deformation and sea-level changes in the northern Chile subduction area (23 S) during the last 330 ky. *Quaternary Science Reviews*, *15*(8-9), 819-831.

Ou, Q., Daout, S., Weiss, J. R., Shen, L., Lazecký, M., Wright, T. J., & Parsons, B. E. (2022). Large-scale interseismic strain mapping of the NE Tibetan Plateau from Sentinel-1 interferometry. *Journal of Geophysical Research: Solid Earth*, *127*(6), e2022JB024176.

Parraguez Landaeta, B. F., Schurr, B., Kummerow, J., Salazar, P., & Sippl, C. (2023, July). Underplating evidence on Mejillones Peninsula zone, Chile. In *XXVIII General Assembly of the International Union of Geodesy and Geophysics (IUGG)*. GFZ German Research Centre for Geosciences.

Pedoja, K., Husson, L., Johnson, M. E., Melnick, D., Witt, C., Pochat, S., ... & Garestier, F. (2014). Coastal staircase sequences reflecting sea-level oscillations and tectonic uplift during the Quaternary and Neogene. *Earth-Science Reviews*, *132*, 13-38.

Plattner, C., Parizzi, A., Carena, S., Rieger, S. M., Friedrich, A. M., Abolghasem, A. M., & DeZan, F. (2022). Long-lived afterslip of the 2013 M w 6.1 Minab earthquake detected by Persistent Scatterer Interferometry along the Irer fault (western Makran-Zagros transition zone, Iran). *Geophysical Journal International*, *229*(1), 171-185.

Ragon, T., & Simons, M. (2023). A Secondary Zone of Uplift Measured After Megathrust Earthquakes: Caused by Early Downdip Afterslip?. *Geophysical Research Letters*, *50*(7), e2022GL101510.

Reutter, K. J., Charrier, R., Götze, H. J., Schurr, B., Wigger, P., Scheuber, E., ... & Belmonte-Pool, A. (2006). The Salar de Atacama Basin: a subsiding block within the western edge of the Altiplano-Puna Plateau. *The Andes: Active Subduction Orogeny*, 303-325.

Rosenau, M., & Oncken, O. (2009). Fore-arc deformation controls frequency-size distribution of megathrust earthquakes in subduction zones. *Journal of Geophysical Research: Solid Earth*, *114*(B10).

Ruiz, S., & Madariaga, R. (2018). Historical and recent large megathrust earthquakes in Chile. *Tectonophysics*, *733*, 37-56.

Sadler, P. M. (1981). Sediment accumulation rates and the completeness of stratigraphic sections. *The Journal of Geology*, *89*(5), 569-584.

Saillard, M., Audin, L., Rousset, B., Avouac, J. P., Chlieh, M., Hall, S. R., ... & Farber, D. L. (2017). From the seismic cycle to long-term deformation: Linking seismic coupling and Quaternary coastal geomorphology along the Andean megathrust. *Tectonics*, *36*(2), 241-256.

Saillard, M., Hall, S. R., Audin, L., Farber, D. L., Hérail, G., Martinod, J., ... & Bondoux, F. (2009). Non-steady long-term uplift rates and Pleistocene marine terrace development along the Andean margin of Chile (31 S) inferred from 10Be dating. Earth and Planetary Science Letters, 277(1-2), 50-63.

Sandwell, D. T., & Wessel, P. (2016). Interpolation of 2-D vector data using constraints from elasticity. *Geophysical Research Letters*, *43*(20), 10-703.

Savage, J. C. (1983). A dislocation model of strain accumulation and release at a subduction zone. Journal of Geophysical Research: Solid Earth, 88(B6), 4984-4996.

Savage, J. C., Gan, W., & Svarc, J. L. (2001). Strain accumulation and rotation in the Eastern California Shear Zone. *Journal of Geophysical Research: Solid Earth*, *106*(B10), 21995-22007.

Schurr, B., Asch, G., Hainzl, S., Bedford, J., Hoechner, A., Palo, M., ... & Vilotte, J. P. (2014). Gradual unlocking of plate boundary controlled initiation of the 2014 Iquique earthquake. *Nature*, *512*(7514), 299-302.

Schurr, B., Asch, G., Rosenau, M., Wang, R., Oncken, O., Barrientos, S., ... & Vilotte, J. P. (2012). The 2007 M7. 7 Tocopilla northern Chile earthquake sequence: Implications for along-strike and downdip rupture segmentation and megathrust frictional behavior. *Journal of Geophysical Research: Solid Earth*, *117*(B5).

Schwanghart, W., & Scherler, D. (2014). TopoToolbox 2–MATLAB-based software for topographic analysis and modeling in Earth surface sciences. *Earth Surface Dynamics*, *2*(1), 1-7.

Shackleton, N. J., Sánchez-Goñi, M. F., Pailler, D., & Lancelot, Y. (2003). Marine isotope substage 5e and the Eemian interglacial. *Global and Planetary change*, *36*(3), 151-155.

Shirzaei, M., Bürgmann, R., Oncken, O., Walter, T. R., Victor, P., & Ewiak, O. (2012). Response of forearc crustal faults to the megathrust earthquake cycle: InSAR evidence from Mejillones Peninsula, Northern Chile. *Earth and Planetary Science Letters*, *333*, 157-164.

Song, T. R. A., & Simons, M. (2003). Large trench-parallel gravity variations predict seismogenic behavior in subduction zones. *Science*, *301*(5633), 630-633.

Starke, J., Ehlers, T. A., & Schaller, M. (2017). Tectonic and climatic controls on the spatial distribution of denudation rates in Northern Chile (18 S to 23 S) determined from cosmogenic nuclides. *Journal of Geophysical Research: Earth Surface*, *122*(10), 1949-1971.

Strecker, M. R., Alonso, R. N., Bookhagen, B., Carrapa, B., Hilley, G. E., Sobel, E. R., & Trauth, M. H. (2007). Tectonics and climate of the southern central Andes. *Annu. Rev. Earth Planet. Sci.*, *35*(1), 747-787.

Tassara, C., Cesca, S., Miller, M., López-Comino, J. Á., Sippl, C., Cortés-Aranda, J., & Schurr, B. (2022). Seismic source analysis of two anomalous earthquakes in Northern Chile. *Journal of South American Earth Sciences*, *119*, 103948.

van Dinther, Y., Preiswerk, L. E., & Gerya, T. V. (2019). A secondary zone of uplift due to megathrust earthquakes. *Pure and Applied Geophysics*, *176*, 4043-4068.

Victor, P., Oncken, O., Sobiesiak, M., Kemter, M., Gonzalez, G., & Ziegenhagen, T. (2018). Dynamic triggering of shallow slip on forearc faults constrained by monitoring surface displacement with the IPOC Creepmeter Array. *Earth and Planetary Science Letters*, *502*, 57-73.

Victor, P., Sobiesiak, M., Glodny, J., Nielsen, S. N., & Oncken, O. (2011). Long-term persistence of subduction earthquake segment boundaries: Evidence from Mejillones Peninsula, northern Chile. *Journal of Geophysical Research: Solid Earth*, *116*(B2).

Walk, J., Stauch, G., Reyers, M., Vásquez, P., Sepúlveda, F. A., Bartz, M., ... & Lehmkuhl, F. (2020). Gradients in climate, geology, and topography affecting coastal alluvial fan morphodynamics in hyperarid regions–The Atacama perspective. *Global and Planetary Change*, *185*, 102994.

Wang, K., Hu, Y., & He, J. (2012). Deformation cycles of subduction earthquakes in a viscoelastic Earth. Nature, 484(7394), 327-332.

Weiss, J. R., Walters, R. J., Morishita, Y., Wright, T. J., Lazecky, M., Wang, H., ... & Parsons, B. (2020). High-resolution surface velocities and strain for Anatolia from Sentinel-1 InSAR and GNSS data. *Geophysical Research Letters, 47*(17), e2020GL087376.

Wells, R. E., Blakely, R. J., Sugiyama, Y., Scholl, D. W., & Dinterman, P. A. (2003). Basin-centered asperities in great subduction zone earthquakes: A link between slip, subsidence, and subduction erosion?. *Journal of Geophysical Research: Solid Earth*, *108*(B10).

Wessel, P., Smith, W. H. F., Scharroo, R., Luis, J. F., & Wobbe, F. (2013). Generic Mapping Tools: Improved version released. EOS Transactions AGU, 94, 409–410.

Wright, T. J., Parsons, B. E., & Lu, Z. (2004). Toward mapping surface deformation in three dimensions using InSAR. *Geophysical Research Letters*, *31*(1).